

Guiding experimental discovery of rare-earth-free magnetic materials through the development of a comprehensive database

Masahiro Sakurai,^{1,*} Renhai Wang,^{2,3} Timothy Liao,^{1,4} Chao Zhang,² Huaijun Sun,² Yang Sun,² Haidi Wang,² Xin Zhao,² Songyou Wang,^{5,6} Balamurugan Balasubramanian,⁷ Xiaoshan Xu,⁷ David J. Sellmyer,⁷ Vladimir Antropov,⁶ Jianhua Zhang,² Cai-Zhuang Wang,^{2,6,†} Kai-Ming Ho,^{2,6} and James R. Chelikowsky^{1,4,8}

¹*Center for Computational Materials, Oden Institute for Computational Engineering and Sciences, The University of Texas at Austin, Austin, Texas 78712, USA*

²*Department of Physics and Astronomy, Iowa State University, Ames, Iowa 50011, USA*

³*Department of Physics, University of Science and Technology of China, Hefei 230026, China*

⁴*Department of Physics, The University of Texas at Austin, Austin, Texas 78712, USA*

⁵*Department of Optical Science and Engineering, Fudan University, Shanghai, 200433, China*

⁶*Ames Laboratory, U.S. Department of Energy, Ames, Iowa 50011, USA*

⁷*Nebraska Center for Materials and Nanoscience and Department of Physics and Astronomy, University of Nebraska, Lincoln, Nebraska, 68588, USA*

⁸*McKetta Department of Chemical Engineering, The University of Texas at Austin, Austin, Texas 78712, USA*

(Dated: July 30, 2020)

We develop an open database that provides a large array of datasets specialized for magnetic compounds as well as magnetic clusters, with focus on rare-earth-free magnets. Available datasets include (i) the crystallography, (ii) the thermodynamic properties, such as the formation energy, and (iii) the magnetic properties that are essential for permanent-magnet design. Our database features a large number of stable and metastable structures discovered through our adaptive genetic algorithm (AGA) searches. Some of these AGA structures have better magnetic properties in comparison to those of the existing rare-earth-free magnets and the theoretical structures in other databases. Our database places particular emphasis on the site-specific magnetic data, which are obtained by high-throughput first-principles calculations. Such site-resolved data are indispensable for machine-learning modelings. We illustrate how our data-intensive methods promote efficiency of the experimental discovery of new magnetic materials. Our database provide massive datasets that facilitate an efficient computational screening, machine-learning-assisted design, and the experimental fabrication of new promising magnets.

I. INTRODUCTION

Magnet plays an important role in a wide range of devices and is one of the key materials in modern technologies, such as cell phones, computers, electrical vehicles, wind turbines, medical equipments and so on. A major component of prototypical permanent magnet is a 3d transition metal (typically iron), which provides a large amount of saturation magnetization. Most of high-performance permanent magnets contain a small dose of rare-earth elements, such as neodymium (Nd) and dysprosium (Dy). These “strategic” elements are of particular importance to improve its performance in permanent-magnet applications [1–5].

The demand for rare-earth-based high-performance permanent magnets grows year after year, putting economical and political pressure on the supply of rare-earth elements. Concerns about the potential supply shortage of rare-earth elements have stimulated theoretical and experimental efforts to improve the magnetic properties without relying on rare earths [6, 7]. Similarly,

the permanent-magnet materials currently being used or considered as potential candidates for recording-media applications contain expensive Pt [8, 9]. The search for new permanent-magnet materials free from critical rare earths and expensive Pt is also intriguing from the view point of data-storage applications.

For designing a high-performance permanent magnet without rare-earth elements, key magnetic properties to be optimized are: (i) the saturation magnetic polarization, J_s , (ii) the magnetic anisotropy energy (MAE) sufficient to induce high coercivity and a large maximum energy product, and (iii) the Curie temperature, T_c . It is highly desirable to maximize these three quantities simultaneously for the use in permanent-magnet applications. The three key magnetic properties are the macroscopic parameters that originate from the microscopic (“site-specific”) magnetic properties, such as the local magnetic moments, the on-site spin-orbit energies for anisotropy, and the pairwise magnetic exchange coupling parameters. It is, thus, essential to control these site-specific magnetic properties for optimizing the performance of permanent magnet.

With advances in high-throughput first-principles calculations, there has been several efforts to combine first-principles calculations with data science approaches, such as machine learning [10, 11]. These efforts include the construction of an open database of materials, such as

* sakurai@issp.u-tokyo.ac.jp; Present address: The Institute for Solid State Physics, The University of Tokyo, Kashiwa, Chiba 277-8581, Japan

† wangcz@ameslab.gov

AFLOW [12, 13], Materials Project [14, 15], the Open Quantum Materials Database (OQMD) [16, 17], and the NOMAD repository [18]. These databases cover a wide class of materials and provide basic material properties, such as the elastic properties, the thermodynamic properties, and the band gap energies. However, none of them specifically focuses on the magnetic materials. Although several open databases [19–21] provide a small set of magnetic data for selected magnets, there is a distinct lack of the site-specific magnetic data, which are essential for the permanent-magnet design. In spite of its importance, the availability of dataset for magnetic clusters remains very sparse.

Here, we develop an open database of magnetic materials [22] to facilitate data-intensive design of new rare-earth-free magnets. The remaining of the paper is organized as follows. In Sec. II, we present our theoretical framework to collect and generate a variety of materials data. In Sec. III, we give an overview of our database, along with statistics. In Sec. IV, we describe the details of available datasets, followed by notes about the unique features of our database in Sec. V. We illustrate in Sec. VI how our data-intensive methods promote efficiency of the experimental discovery of new magnetic materials. We give a perspective on the applications of our database in data science in Sec. VII, and summarize this work in Sec. VIII.

II. METHODS FOR DATA GENERATION

A. Collection and generation of magnetic materials

We first collect Fe-based structures listed on the Materials Project database [15]. These include binary (Fe- X), ternary (Fe- X - X'), and quaternary (Fe- X - X' - X'') compounds, where X represents non-magnetic (B, C, N, Al, Si, P, S, Ga, Ge, As, and Se) and magnetic (Ti, V, Cr, Mn, Co, Ni, Cu, Zn, Y, Zr, Nb, and Mo) species across the periodic table. In a similar way, we collect Mn-based, Co-based, and Ni-based structures from Materials Project.

We also employ the adaptive genetic algorithm (AGA) [23, 24] to discover new stable and metastable structures in broader configuration space than the Materials Project database. Our AGA search consists of a conventional genetic algorithm (GA) process and an “adaptive” process. In a conventional GA process, we use the auxiliary classical potential to optimize trial structures in a search pool. In an adaptive process, we update adaptively the auxiliary potential by matching it to the density-functional theory (DFT) results on a subset of the optimized structures in the pool [25]. This strategy makes it possible to explore broad configuration space very efficiently with keeping the accuracy of structure prediction. At every AGA step, trial structures are “filtered” in the spirit of Darwin’s theory of evolution. Structures with lower energies are reserved for the next step, whereas structures

with higher energies are substituted by new ones that are generated from low-energy parent structures. After dozens of AGA iterations, a search pool gets populated densely by low-energy off-spring structures.

The formation energies of AGA-discovered structures are within a reasonable energy range above the convex hull, as shown for Zr-Co and Fe-Co-N systems [26, 27]. Moreover, our AGA search is a useful method to identify new structures in experiments, as demonstrated for Co-N [28–30] and Li-Ni-B [31, 32] systems. The latest version of our AGA code is implemented with an advanced search technique, which we call “symmetry-AGA,” allowing us to narrow down search space and to discover new structures with a particular crystal symmetry.

B. First-principles calculations

We perform first-principles calculations to compute the thermodynamic and magnetic properties of the magnetic materials collected from Materials Project and generated by the AGA. Our first-principles calculations are based on the DFT [33, 34] combined with the projector-augmented wave (PAW) method [35]. We adopt a generalized gradient approximation (GGA) [36] for the exchange-correlation functional. For crystals, we use a plane-wave basis set with a cutoff energy of 65 Ry to expand the valence wave functions. The Monkhorst-Pack scheme [37] is used to generate a k -point grid to perform Brillouin-zone integration. A k -point resolution of $2\pi \times 0.025 \text{ \AA}^{-1}$ is used for spin-polarized calculations. All plane-wave calculations are carried out by using VASP [38, 39] and QUANTUM ESPRESSO [40].

The MAE is defined as the total-energy difference between two magnetic configurations. The magnetic anisotropy constant in the lowest order, K , is written as

$$K^{a-c} = (E_a - E_c)/V. \quad (1)$$

Here, E_a (E_c) is the total energy for the magnetization oriented along the crystallographic a (c) axis, and V denotes the volume of a system. For uniaxial systems, positive K^{a-c} value means that the c axis is the magnetization direction of the lowest energy, called the magnetic easy axis. When K^{a-c} is negative, the system has the easy axes in the ab plane. We incorporate the spin-orbit interactions in MAE calculations, where we use a finer mesh size of $2\pi \times 0.016 \text{ \AA}^{-1}$ to achieve better convergence.

We adopt a static linear-response approach using Liechtenstein’s formula [41] to compute the magnetic exchange coupling parameters, J_{ij} . In this approach, we employ the linear muffin-tin orbital (LMTO) basis set [42] and the atomic sphere approximation (ASA) to the Green’s function method [43]. On top of the LMTO-ASA results, we solve the classical Heisenberg model to estimate the Curie temperature, T_c , within the mean-field approximation. The momentum-space exchange coupling parameters, $J(q)$, are converted into the real-space

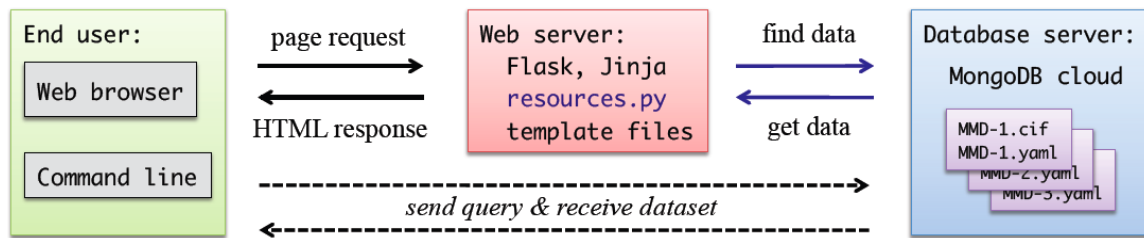


FIG. 1. A dataflow diagram of our Magnetic Materials Database [22].

ones, $J(r)$, by the inverse Fourier transform. We use 41 points on an elliptical contour in the complex plane to carry out the energy integrals involved in the exchange parameter calculations. We use a k -point mesh with a resolution of $2\pi \times 0.025 \text{ \AA}^{-1}$ as well. All T_c and J_{ij} calculations are done by using QUESTAAL [44].

C. Magnetic clusters

Magnetic clusters are constructed as fragments of bulk crystals, as has been done for Co_3N [45]. We also build icosahedral and cuboctahedral clusters for Fe, Co, and Ni [46–48], both of which have locally a closed-packed atomic coordination. Cluster geometry can be characterized by the atomic arrangement around the cluster core, the atomic coordination in a “mantle” region, and its surface structure (faceted or not). We carry out structural relaxations [49–51] for all magnetic clusters until a residual force is less than 0.01 Ry/a.u.

For magnetic clusters, we solve the Kohn-Sham equations on a uniform grid in *real space* as implemented in the PARSEC code [52–54]. The GGA-PBE functional is adopted for real-space DFT calculations. The Laplacian operator in the kinetic-energy term is expanded by using a high-order finite-differencing scheme. A grid spacing of 0.3 a.u. (approximately 0.16 Å) is sufficient to achieve the convergence of the total energy to within 1 meV/atom for 3d transition-metal systems [45–48, 55]. We employ a spherical domain as a boundary condition to simulate an isolated cluster. The wave functions are sampled inside the domain and vanish beyond the domain boundary (typically 10 a.u. away from the outermost atom of a cluster). A notable feature of our real-space DFT code, PARSEC, is the use of a subspace filtering technique that exploits Chebyshev polynomials [56–58]. This filtering algorithm allows us to avoid explicit diagonalizations during the self-consistent field cycle.

III. DATABASE OVERVIEW

A. Data organization

Figure 1 illustrates the dataflow of our Magnetic Materials Database [22]. A data entry for an individual mag-

netic material is created with two file formats: (i) Crystallographic Information File (CIF) [59] and (ii) YAML (that stands for “YAML Ain’t Markup Language” [60]). The CIF is a standard format in materials science to archive the crystallographic information. We use YAML, a popular data-serialization scheme, to store the computational results for the thermodynamic and magnetic properties. Two data files are processed with Python [61], an object-oriented programming language, with the help of the Pymatgen libraries [62]. All the data are integrated into one location, building an online master database on the MongoDB cloud [63]. Upon finding new structures as well as finishing first-principles calculations, we append new data to the master database.

B. Database statistics

Table I summarizes the number of entries of our Magnetic Materials Database [22]. For crystal systems, a total of 3,826 entries are registered at the time of submission. These entries include the crystal structures taken from the Materials Project database [15] and those generated from our AGA techniques. By cross-checking all of the uploaded structures, we find a lesser degree of overlap between the two groups. This is because our AGA search yields not only stable compounds but also a lot of metastable structures, which are distributed in a wide range of chemical compositions. For magnetic clusters, our database contains a total of 1,163 entries. Our magnetic clusters are elemental, binary, and ternary clusters,

TABLE I. The number of magnetic materials that are collected from the Materials Project (MP) database, discovered by our adaptive genetic algorithm (AGA), and from our cluster studies. The number in the parentheses denotes the overlap between the two groups.

System	Crystal			Cluster
	MP	AGA	(overlap)	
Mn-based	584	0	(0)	0
Fe-based	787	290	(7)	929
Co-based	714	594	(41)	151
Ni-based	832	6	(0)	73

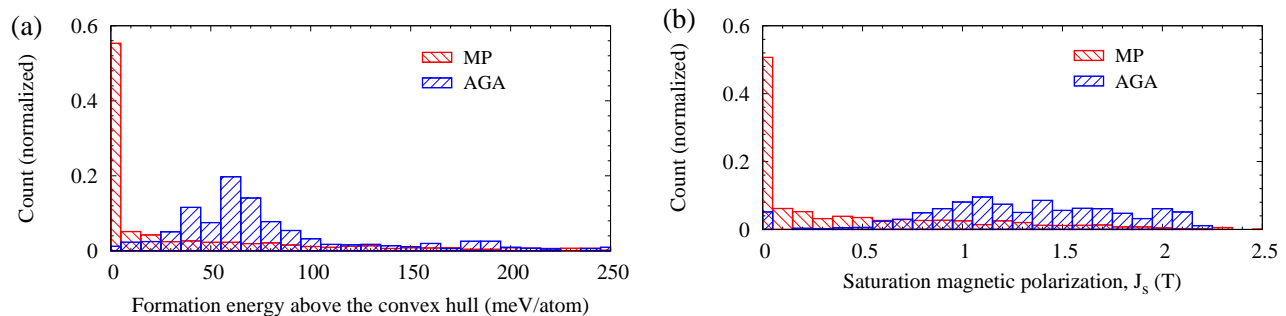


FIG. 2. Histogram charts that compare the population of two sets of magnetic materials with respect to (a) the formation energy above the convex hull and (b) the saturation magnetic polarization. The one group is from the Materials Project (MP) database, and the other group is from our adaptive genetic algorithm (AGA) searches.

TABLE II. The number of entries and its percentage to the total for seven crystal systems.

Crystal system	Entries	Percentage
Triclinic	243	6%
Monoclinic	526	14%
Orthorhombic	934	24%
Tetragonal	594	16%
Trigonal	342	9%
Hexagonal	421	11%
Cubic	766	20%

with sizes ranging from 5 to 22 Å in diameter. Our clusters have atomic sites of 9–490 with various Fe (Co) content.

Statistical data for crystal systems are given in Tables II and III. Our database contains magnetic materials for all seven crystal systems. Binary and ternary compounds account for 36 % and 62 % of the total number of entries, respectively. For binary (ternary) compounds, we have 114 (611) different combinations of two (three) elements. Each system is populated by dozens of structures with various chemical compositions (stoichiometry), with Fe-rich and Co-rich structures being in the majority.

Figures 2(a) and (b) compare the population of magnetic materials with respect to the stability (the formation energy above the convex hull) and the magnetic property (the saturation magnetic polarization), respectively. Structures from Materials Project are very stable, with a sharp peak for the formation energies above the convex hull of 0–5 meV/atom. However, such stable structures have a very small magnetization value, as shown in Fig. 2(b). Most of our AGA structures have the formation energies above the convex hull of less than 200 meV/atom, with a broad peak centered around 60 meV/atom. It is evident in Fig. 2(b) that our AGA structures have larger magnetization values than Materials Project structures.

TABLE III. The number of entries and the number of combination of three elements for elemental system, binary, ternary, and quaternary compounds.

System	Entries	Combinations
Elemental	59	15
Binary	1,372	114
Ternary	2,349	611
Quaternary	46	35

C. Data availability

We provide end users with our data through our website at <https://magmatdb.herokuapp.com> (university domain?). Our web server applications are developed with the Flask framework [64] powered with the Jinja template engine [65], as shown in the middle of Fig. 1. Our web applications are deployed on Heroku [66], a cloud-based application platform, where we use (i) Python scripts to load datasets from the master database, (ii) numerical libraries to carry out mathematical operations, and (iii) the Matplotlib utilities [67] to visualize data. These framework makes it possible to serve an automated, dynamic web page as well as to draw diagrams on demand. All the diagrams generated on our web applications are available in the Portable Network Graphics (png) format. Page viewers can download individual images.

IV. DESCRIPTION OF DATASET

In this section, we describe the details of datasets on our Magnetic Materials Database [22]. Available data include crystallographic data, the thermodynamic properties, macroscopic and microscopic (“site-specific”) magnetic properties, computational details, and references, for crystalline phases and nanoclusters.

TABLE IV. The Crystallographic data of Fe_5CoN_2 .

Key	Value
Entry ID	MMD-17
Crystal system	orthorhombic
Space group	Amm2 (No. 38)
Chemical formula	Fe_5CoN_2
Formula unit(s)	2
Lattice parameters	$a = 3.834, b = 3.764, c = 11.162 \text{ \AA}$ $\alpha = 90.0, \beta = 90.0, \gamma = 90.0 \text{ (deg.)}$
Volume	161.063 \AA^3
Density	7.550 g/cm^3
Atomic positions ^a	Fe 2a (0.00000, 0.00000, 0.18331) Fe 2a (0.00000, 0.00000, 0.49958) Fe 2b (0.50000, 0.00000, 0.34649) Fe 2b (0.50000, 0.00000, 0.67654) Fe 2b (0.50000, 0.00000, 0.99567) Co 2a (0.00000, 0.00000, 0.83344) N 2a (0.00000, 0.00000, 0.00000) N 2b (0.50000, 0.00000, 0.17748)
Source	AGA search

^a Element symbol, Wyckoff position, and fractional coordinates.

A. Crystallography

Our database provides the crystallographic data for all crystals. Available crystallographic dataset includes crystal system, space group (the Hermann-Mauguin notation and the international number [68]), chemical composition in a reduced formula, unit cell volume, lattice parameters, and atomic positions (Wyckoff positions and fractional coordinates). Table IV lists an example dataset of an Fe_5CoN_2 compound, which is discovered through our AGA search. We assign an entry ID of MMD-17 to this compound. On our database, the lattice parameters and atomic positions are available in various file formats: CIF, POSCAR (an input file format for VASP), an input file format for LAMMPS (a classical molecular dynamics code [69]), JSON (JavaScript Object Notation) [70], and YAML.

B. Thermodynamic properties

The thermodynamic properties, such as the formation energy, are tabulated and visualized on the web page for an individual structure. Based on DFT calculations, the formation energies are calculated with respect to a linear combination of the total energies of reference elemental phases.

As an example, we show in Fig. 3 the compositional phase diagram of an Fe-Si system, where the calculated formation energies are plotted as a function of the atomic fraction of Fe. In Fig. 3, a set of lines connecting the sta-

TABLE V. Example dataset for the thermodynamic and magnetic properties of Fe_5CoN_2 (MMD-17).

Key	Value
Thermodynamic properties	
Formation energy (vs. elemental phases)	-14.7 meV/atom
Formation energy above convex hull	$+77.1 \text{ meV/atom}$
Magnetic properties	
Total magnetic moment	$23.88 \mu_B/\text{cell}$
Magnetic saturation polarization, J_s	1.73 T
Magnetic easy axis	c
Magnetic anisotropy constant, K^{a-c}	1.47 MJ/m^3
Magnetic anisotropy constant, K^{b-c}	2.56 MJ/m^3
Magnetic anisotropy constant, K^{b-a}	1.09 MJ/m^3
Magnetic hardness parameter ^a , κ	0.79
Curie temperature, T_c	1534 K

^a See text for definition.

ble phases forms a convex hull, which represents a plausible lower limit in the formation energy of this system. It is evident that the great majority of our AGA structures are distributed in the vicinity of the convex hull (within $\sim 50 \text{ meV/atom}$ above the hull) over a wide range of the Fe concentration. Such low-energy metastable structures are possible candidate phases, which can be reached out by using advanced fabrication techniques as we will illustrate in Sec. VI.

A compositional phase diagram of a ternary system can be shown as a projection of a three-dimensional energy curve onto two dimensions. Figure 4(a) shows the triangular phase diagram of an Fe-Co-N system. A two-dimensional projection of the minimum-energy surface, indicated by the black solid lines in Fig. 4(a), divides the compositional space into the Gibbs triangles. The for-

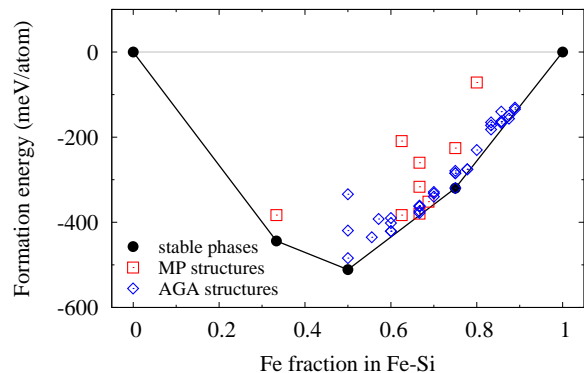


FIG. 3. Phase diagram of a binary Fe-Si system. The formation energies are plotted as a function of the Fe content. Crystal structures are taken from Materials Project (MP) and discovered through our adaptive genetic algorithm (AGA). The solid lines that connect stable phases represent a boundary in a compositional phase diagram, called the convex hull.

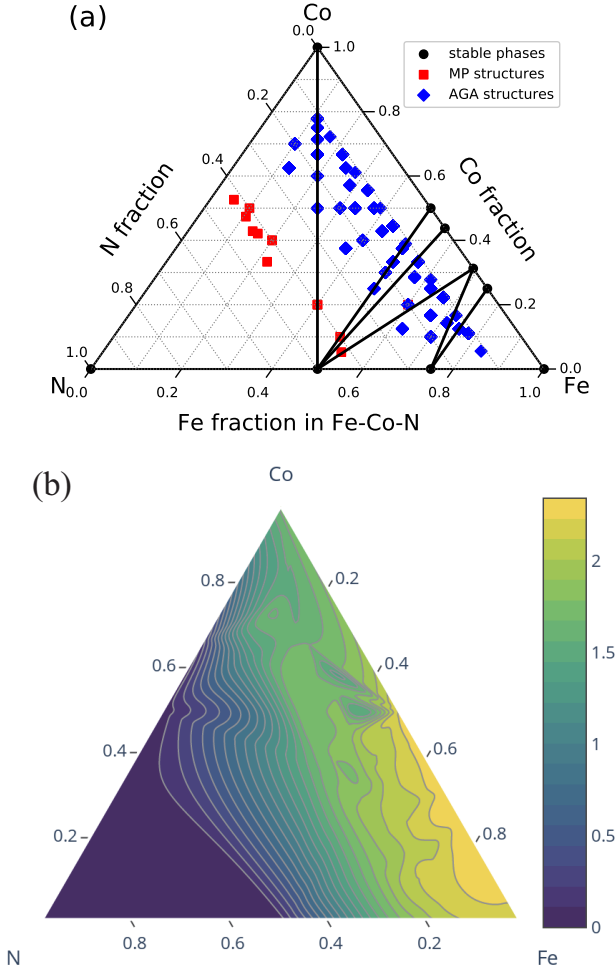


FIG. 4. (a) Compositional phase diagram of a ternary Fe-Co-N system. Crystal structures are taken from Materials Project (MP) and discovered through our adaptive genetic algorithm (AGA). The solid lines indicate the convex hull, a two-dimensional projection of the minimum-energy surface. (b) A contour plot of the magnetic saturation polarization in an Fe-Co-N system.

mation energies above the convex hull of the structures from Materials Project (13 entries) are in the range of 0.1–0.4 eV/atom, whereas those of our AGA-discovered Fe- and Co-rich structures (258 out of 259 entries) are less than 0.1 eV/atom. The MMD-17 Fe_5CoN_2 phase is among such AGA structures, and its formation energy is listed in Table V.

In addition to a ternary phase diagram of the formation energy, we provide a ternary contour map of the magnetic saturation polarization as shown in Fig. 4(b). Contour lines and color gradation help you analyze the landscape of the magnetic saturation polarization in a ternary system, along with the stability.

C. Macroscopic magnetic properties

Our database focuses on three macroscopic magnetic properties as key parameters for permanent-magnet design: (i) the magnetic saturation polarization, J_s , in units of Tesla, (ii) the magnetic anisotropy constant, K , in units of MJ/m³, and (iii) the Curie temperature, T_c , in units of Kelvin. The magnetic saturation polarization is related to the saturation magnetization, M_s , through $J_s = \mu_0 M_s$, with μ_0 being the permeability of vacuum. These magnetic properties, along with related magnetic properties, are tabulated on an individual web page. An example dataset is given in Table V.

The magnetic saturation polarization and the total magnetic moment (Bohr magneton, μ_B , per unit cell, neglecting the orbital magnetic moments) are available for all structures. For structures with large magnetization ($J_s \geq 1$ T), we determine the magnetic anisotropy constant, K^{a-c} , and the magnetic easy axis. In particular, our database provides multiple K values (K^{a-c} , K^{b-c} , and K^{b-a}) for orthorhombic, monoclinic, and triclinic crystal systems, as listed in Table V for the orthorhombic Fe_5CoN_2 phase (MMD-17). Our magnetic dataset also includes a dimensionless parameter,

$$\kappa = \sqrt{|K|/(\mu_0 M_s^2)}, \quad (2)$$

called magnetic hardness parameter. The parameter, κ , has been recognized as a useful criterion to assess the potential of magnetic materials as a permanent magnet [3, 71]. The Curie temperature, T_c , is estimated for structures with $J_s \geq 1$ T and $K \geq 1$ MJ/m³.

Figure 5(a) shows the comparison of the theoretical and experimental values of the saturation magnetic polarization, J_s . The calculated J_s values agree well with the experimental values in a wide range of J_s . In particular, there is an excellent agreement for materials with $J_s > 1$ T, making it possible to capture the J_s behaviour of Fe-based and Co-based systems on an equal footing.

In Fig. 5(b), we plot our theoretical values of the magnetic anisotropy constant, K , for several existing rare-earth-free magnets. Overall, there is a good agreement between theory and experiment. We find significant underestimation of K about a factor of about 2 for some exceptional systems with a large K , such as YCo_5 . Still, our DFT results agree with the earlier work that reports a similar level of underestimation by the DFT framework [72].

Figure 5(c) shows the Curie temperature, T_c , calculated for prototypical magnets. A percentage error between experimental values and our theoretical values is less than 20 % for most of the systems. We confirm that our LMTO-ASA approach combined with the mean-field approximation works well for estimating the T_c for various kinds of Fe-based and Co-based alloys.

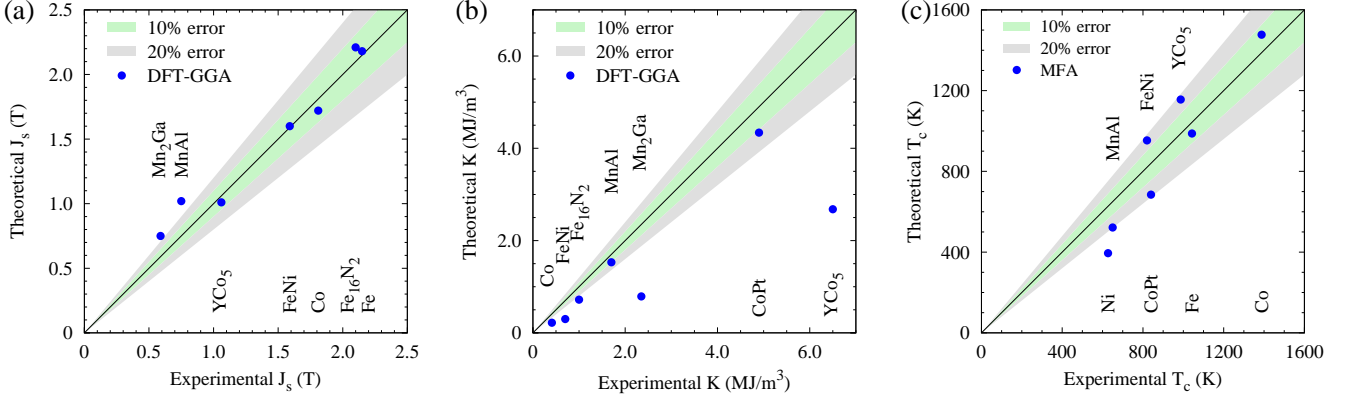


FIG. 5. Comparison of the theoretical and experimental values of (a) the saturation magnetic polarization, J_s , (b) the magnetic anisotropy constant, K , and (c) the Curie temperature, T_c . We carry out DFT-GGA calculations for computing J_s and K , whereas we adopt the mean-field approximation (MFA) to estimate T_c . The reference materials are given in each plot. The shaded areas indicate the relative errors to the experimental values.

D. Site-specific magnetic properties

Our database places a strong emphasis on the site-specific magnetic properties: (i) the local magnetic moments, (ii) the site-resolved spin-orbit coupling anisotropy energies, and (iii) the pairwise magnetic exchange coupling parameters. These microscopic quantities are key parameters for controlling the macroscopic magnetic properties, as well as for building machine-learning models for permanent-magnet design.

Figures 6(a) and 6(b) show the local magnetic moments, m_i , and the site-resolved spin-orbit coupling anisotropy energies, E_i^{so} , respectively, of the Fe_5CoN_2 phase tagged with MMD-17 (Table IV). The local magnetic moment is defined as

$$m_i = \int_{\Omega_i} [\rho_{\uparrow}(\vec{r}) - \rho_{\downarrow}(\vec{r})] d^3r. \quad (3)$$

Here, $\rho_{\uparrow(\downarrow)}$ denotes the electron density of the majority (minority) spin and Ω_i is a spherical domain centered on an atom i . It is evident that these microscopic magnetic parameters vary from site to site. The site-resolved magnetic data is indispensable for the detailed analysis of the macroscopic magnetic properties as well as data-intensive design of new permanent magnets.

In Fig. 7(a), we visualize the pair-resolved magnetic exchange coupling parameters, J_{ij} , in a two-dimensional heat map. The magnitude of the exchange coupling between site i and j is shown on each colored cell. Here, we take the Fe_5CoN_2 phase (entry ID of MMD-17) as an example. The plot is helpful to understand which pair is responsible for a large magnetic coupling.

Figure 7(b) shows the spatial dependence of J_{ij} in Fe_5CoN_2 (MMD-17). We plot the J_{ij} values in bcc Fe and hcp Co for comparison. It is evident that magnetic interactions between different types of atomic sites have different spatial behavior. Large magnetic couplings oc-

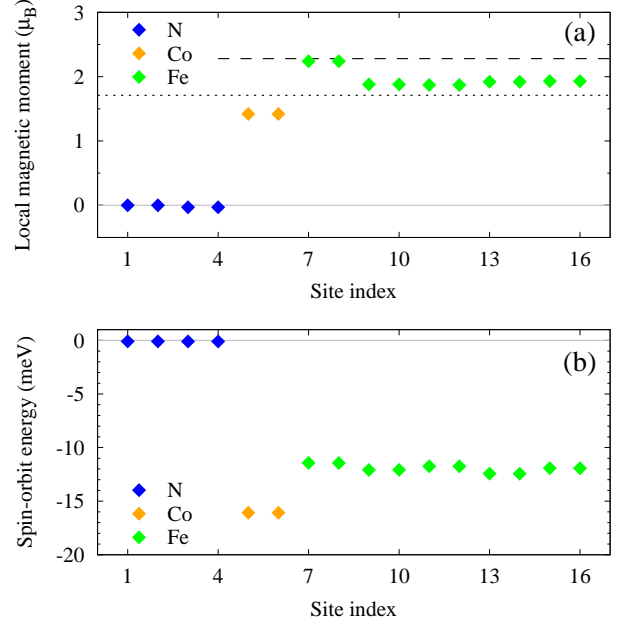


FIG. 6. Examples of the site-specific magnetic properties available on our Magnetic Materials Database [22]. (a) The local magnetic moments, m_i in units of μ_B/atom , of an atomic site i for Fe_5CoN_2 [an entry ID of MMD-17 (Table IV)]. The dashed and dotted lines indicate the values in bcc Fe and hcp Co, respectively. (b) The site-resolved spin-orbit coupling anisotropy energies, E_i^{so} , in units of meV, of Fe_5CoN_2 (MMD-17). **Figure (b) will be updated.**

cur between Fe-Fe and Fe-Co pairs in Fe_5CoN_2 , whereas the Co-Co couplings of this system are highly suppressed in comparison to those in hcp Co. The coupling parameters practically vanish when the neighbor distance goes beyond two lattice constants ($\sim 8 \text{ \AA}$).

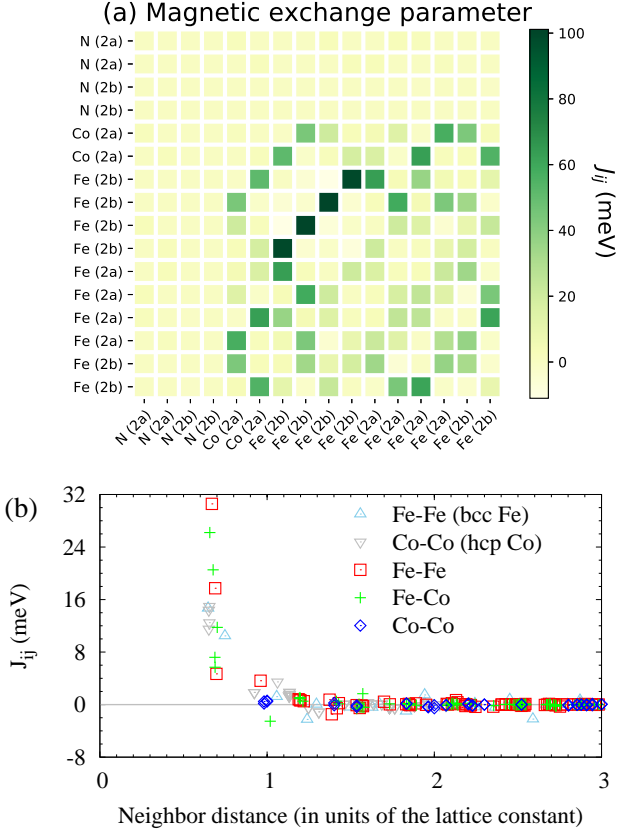


FIG. 7. Examples of pairwise magnetic properties available on our Magnetic Materials Database [22]. (a) The magnetic exchange coupling parameters, J_{ij} , between two atomic sites in Fe_5CoN_2 (MMD-17). (b) Individual J_{ij} values as a function of the neighbor distance scaled with the lattice constant of Fe_5CoN_2 ($a = 3.834 \text{ \AA}$). The J_{ij} values in bcc Fe and hcp Co are also shown for comparison.

E. Cluster data

In addition to massive datasets for crystalline systems, our database provides a large amount of data for magnetic nanoclusters. In spite of its importance, cluster data is extremely sparse because most of the open databases focus only on magnetic crystals. The available datasets include (i) structural information, such as chemical species and their atomic position in the Cartesian coordinates, (ii) stability, such as the binding energy, and (iii) the magnetic properties, such as the total and local magnetic moments. For magnetic clusters, a total of 1,153 entries have been registered so far (Table I).

Figure 8 shows the spatial variation of the local magnetic moments in Co clusters with three different atomic coordinations [hcp, bcc, and icosahedral (fcc-like)]. Overall, the local magnetic moments grow steadily as going from the interior toward the surface. The local magnetic moments in a core region are a bulk-like value ($\sim 1.7 \mu_B$), whereas those near the surface are greatly enhanced because surface atom has fewer neighbors, re-

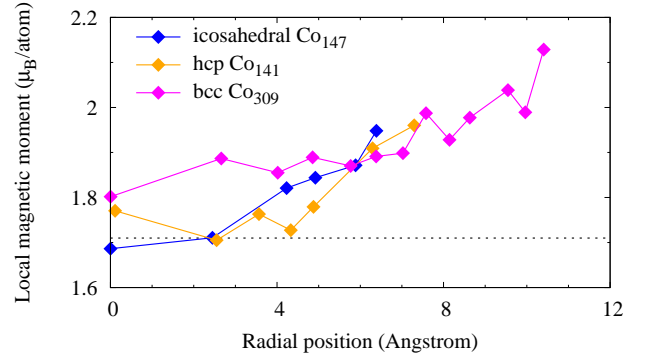


FIG. 8. Evolution of the local magnetic moments in Co clusters with different sizes and local atomic coordinations. The dotted line indicates the value of Co bulk (hcp).

sulting in a stronger spin polarization [46–48].

F. Computational details and references

In addition to the structural and magnetic properties, the computational details and references are given on our database web pages. Computational details include notes about the methodology and numerical parameters, such as convergence criteria and k -point grids. Reference entries are original research papers and/or a uniform resource locator (URL) link to the external databases.

V. UNIQUE FEATURES

A. Friendliness to data science

Our magnetic materials database is specifically designed for the state-of-the-art applications in data science and informatics, such as machine-learning algorithms. A whole set of the above-mentioned data is stored in an online storage at the MongoDB database cloud [63], where all the data items are indexed in a “machine-readable” format (Python Dictionary). The datasets of our database are open to the public through the database web page at <https://magmatdb.herokuapp.com> (domain?). As illustrated in Fig. 1, end users can communicate directly to our online database. End users can request a dataset by sending a query string to the database server using the standard MongoDB scheme. Upon user request, the database server will make a response to return a dataset in a user-friendly format, being suitable for building (or “training”) a machine-learning model.

Our database server is implemented with data-filtering methods so that the server can handle various search keys: element(s), chemical formula, space group number, and the magnetic easy axis. With these search filters, end users can narrow down search results and look up specific structures very easily.

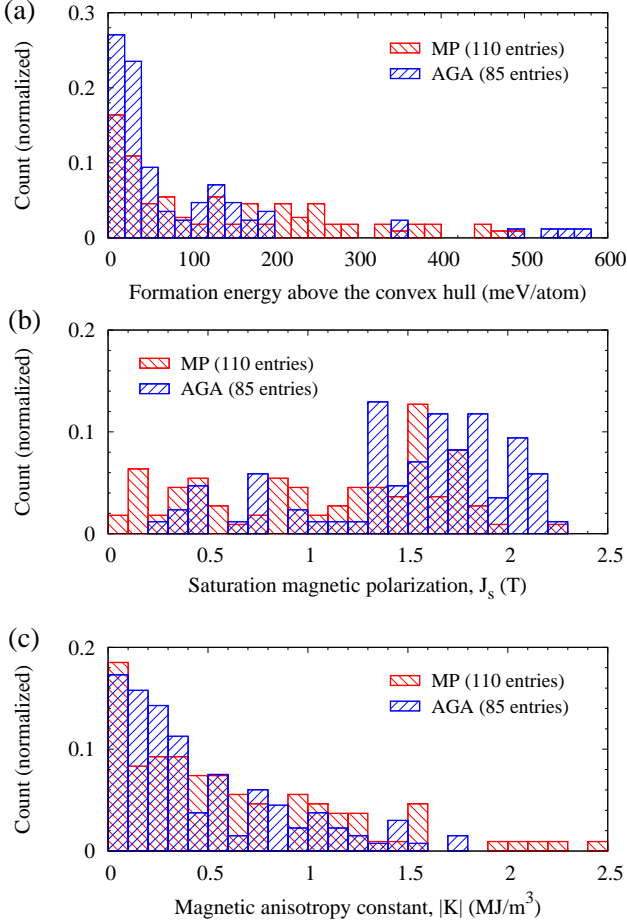


FIG. 9. Histogram charts that compare the population of Fe-based binary structures with respect to (a) the formation energy above the convex hull, (b) the saturation magnetic polarization, and (c) the magnetic anisotropy constant (absolute value). Two sets of structures are from either Materials Project (MP) or our adaptive genetic algorithm (AGA).

B. Promising novel structures from AGA searches

Our database provides a bunch of rare-earth-free structures that are discovered through AGA searches. We note that some of our AGA structures have better magnetic properties *and* are lower in the formation energy (namely, more stable) than the structures on other open databases. In Figs. 9(a)-(c), we compare the population of Fe-based structures with respect to the stability and magnetic properties. Here, we prepare two sets of binary Fe- X structures (with X being B, C, N, Si, P, S, and Ge): one from our AGA search (85 entries) and another from Materials Project (110 entries). The majority of the AGA structures have the formation energies above the convex hull of less than 200 meV/atom. In particular, the AGA group has a high population below 60 meV/atom. In contrast, the MP structures are widely distributed. Figure 9(b) shows that the AGA group is

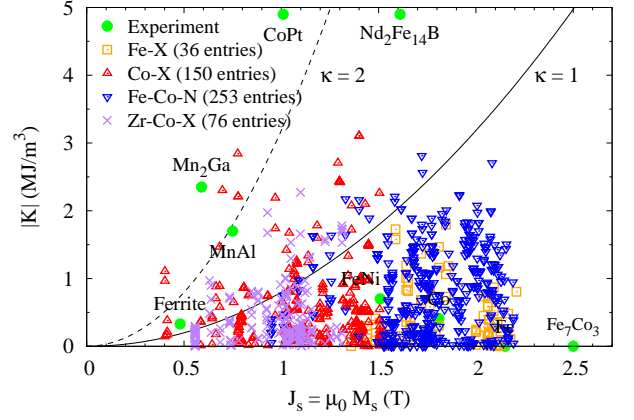


FIG. 10. The magnetic anisotropy constant in its absolute value, $|K|$, versus the saturation magnetic polarization, J_s , for known magnets and AGA-discovered rare-earth-free magnets. The parabolic curves indicate the magnetic hardness parameter, $\kappa = \sqrt{|K|/(\mu_0 M_s^2)}$, of 1 (solid) and 2 (dashed).

populated with structures with a larger saturation magnetic polarization ($1.3 \leq J_s \leq 2.2$ T) in comparison to the MP group. As shown in Fig. 9(c), the two groups are similar in distribution regarding the magnetic anisotropy constant. These analyses mean that the AGA structures are advantageous to exhibit a higher maximum energy product.

We illustrate another strong point of our AGA methodology in Fig. 10, where we plot K versus J_s for AGA structures enriched with Fe and/or Co. We also plot the experimental data of popular magnets for comparison. In terms of the saturation magnetic polarization, the Fe-based and FeCo-based AGA structures are distributed mostly in the range of 1.5–2.2 T, whereas the Co-based and ZrCo-based AGA structures are distributed in a region between 0.5 and 1.5 T. In terms of the magnetic anisotropy, one third of the AGA structures exhibit the decent magnitude of K (≥ 1 MJ/m³) without relying on the critical elements. Moreover, about 10 % of the AGA structures are identified as “hard” magnetic phases. Their magnetic hardness parameters, κ , are greater than 1.0, a recommended value for the use as permanent magnets. In fact, Nd₂Fe₁₄B, the strongest permanent magnet to date, takes a κ value of 1.54. Several AGA structures of Fe-Co-N, Co-X (X =N, Si, Ge), and Zr-Co-X (X =B, C, N) are predicted to have a decent κ value comparable to that of Nd₂Fe₁₄B. These AGA structures are promising candidate phases that yield a sufficient maximum energy product.

VI. GUIDANCE FOR EXPERIMENTAL DISCOVERY

Our AGA searches and advanced electronic-structure calculations guide efficiently the discovery of new

magnetic materials, where experimentalists use non-equilibrium fabrication methods, such as high-pressure sputtering (or cluster deposition) and rapid quenching from the melt (or melt spinning) [7]. Here, we illustrate several examples from our synergistic computational and experimental efforts to discover new rare-earth-free magnetic materials.

A. Screening methods and its application

Our search process consists of three steps. In the first step, we use our AGA methods to explore a bunch of structures across a wide range of chemical compositions. We predict a lot of new stable and metastable intermetallic compounds enriched with Fe and/or Co as possible phases. In the second step, the electronic-structure calculations are performed to evaluate their intrinsic magnetic properties, with focus on finding materials that have the potential to exhibit high J_s , K_1 , and T_c . In the third step, the screened materials with predicted compositions are fabricated using non-equilibrium fabrication methods and subsequently characterized using various structural and magnetic measurements. Our computational screening process helps to accelerate the optimization process during experiments, making it possible to avoid unnecessary experimental steps and reduce the combined search cost.

Our computational screening scheme has been applied to a cobalt-nitride system [29]. Several metastable Co-N compounds are predicted using the AGA. Their intrinsic magnetic properties are estimated using DFT calculations. Figure 11(a) shows the schematic of a rhombohedral crystal structure of a Co_3N compound predicted by the AGA search. The DFT calculations yield $K_1 = 1.39 \text{ MJ/m}^3$, $J_s = 0.83 \text{ T}$, and $T_c = 336 \text{ K}$ for this structure.

These theoretical findings have assisted the synthesis of a set of new Co_3N compounds with desired magnetic properties in the form of nanoparticles using the cluster deposition method [30]. The cluster deposition method enables us to deposit a single phase of rhombohedral Co_3N in the form of nanoparticles on Si (111) substrates. As shown in Fig. 11(b), the experimental x-ray diffraction pattern for the nanoparticles shows the diffraction peaks corresponding to the Co_3N phase and additional peaks from the substrate. There is an excellent agreement between the experimental x-ray spectrum and the simulated spectrum using a Rietveld refinement analysis based on the rhombohedral structure. The experimental lattice parameters, $a = 4.61 \text{ \AA}$ and $c = 13.06 \text{ \AA}$, match with the theoretically predicted values, $a = 4.53 \text{ \AA}$ and $c = 13.06 \text{ \AA}$. With magnetic measurements, we find $K_1 = 1.04 \text{ MJ/m}^3$, $J_s = 0.73 \text{ T}$, and $T_c \sim 450 \text{ K}$ for the rhombohedral Co_3N [30]. These numbers agree reasonably with the values predicted from first-principles calculations [29].

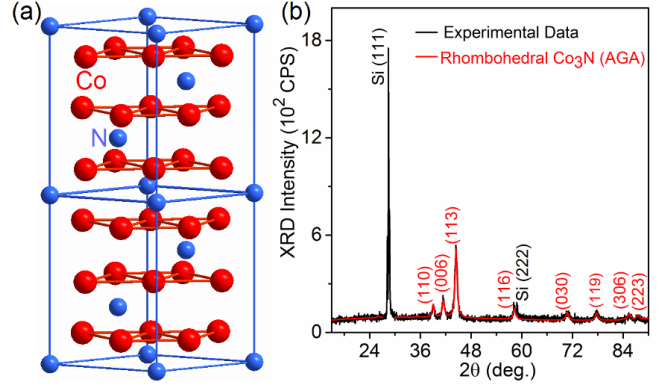


FIG. 11. (a) Schematic of a rhombohedral crystal structure of a Co_3N compound predicted by the AGA search [29]. (b) The experimental x-ray diffraction pattern of the cluster-deposited Co_3N nanoparticles on a Si (111) substrate (black curve) is fitted with the predicted rhombohedral structure using Rietveld analysis (red curve) [30].

B. AGA-assisted crystal structure determination

In experiments, various types of magnetic compounds have been synthesized so far, and some of them can be a complex structure. For such compounds, it remains a challenging and time consuming task to determine the crystal structure and atomic arrangements (Wyckoff positions) using the experimental diffraction patterns. Precise atomic positions are essential to understand the magnetism in new compounds, especially for calculating their intrinsic magnetic properties.

A typical example is the intermetallic compound $\text{Zr}_2\text{Co}_{11}$, which has been fabricated in various ways [73–77]. Figure 12(a) shows a high-resolution transmission electron microscope (HRTEM) image of melt-spun $\text{Zr}_2\text{Co}_{11}$ [26]. Although 2:11 stoichiometry has been determined, it has been difficult for many years to identify the crystal structure of $\text{Zr}_2\text{Co}_{11}$ using the experimental x-ray and electron diffraction patterns. Several complex crystal structures, including orthorhombic, rhombohedral, and hexagonal polymorphs, have been predicted to form near the $\text{Zr}_2\text{Co}_{11}$ stoichiometry [74–77].

Our AGA search is an efficient method to determine the crystal structure of a new compound. The structural determination is based solely on chemical composition. It does not require any assumptions on the Bravais lattice, atom basis, or unit-cell dimensions.

Recently, the AGA search has solved the atomic structure of the rhombohedral $\text{Zr}_2\text{Co}_{11}$ phase [26]. Its space group is found to be $R\bar{3}2$. Its lattice constants are predicted to be $a = 4.69 \text{ \AA}$ and $c = 24.0 \text{ \AA}$. The predicted lattice parameter agrees well with the repeated distance along the c axis ($\sim 24.2 \text{ \AA}$) measured from the HRTEM image of a melt-spun $\text{Zr}_2\text{Co}_{11}$ sample, shown in Fig. 12(a). In the red box of Fig. 12(a), we draw the structural projection and simulated atomic arrangements corresponding to the predicted rhombohedral

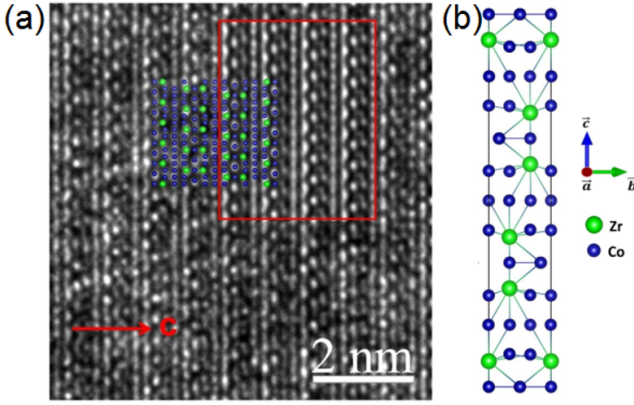


FIG. 12. (a) A high-resolution transmission electron microscope (HRTEM) image of the $\text{Zr}_2\text{Co}_{11}$ compound measured along the $[010]$ zone axis. The red arrow indicates the repeated distance along the c axis. (b) Atomic structure for the rhombohedral $\text{Zr}_2\text{Co}_{11}$ phase solved by the AGA search. Inset within the red box in (a) is the simulated HREM image based on the structural model, and the structure model along the c axis is also laid on top of the experimental HRTEM image [26].

phase [Fig. 12(b)]. The simulated structural model explains well the measured HRTEM image.

DFT calculations are carried out for $\text{Zr}_2\text{Co}_{11}$ in the predicted $R32$ structure, yielding the magnetic properties of $K_1 = 14.2$ Mergs/cm³, $J_s = 10.1$ kG, and $T_c = 709$ K. These are in good agreement with the measured values ($K_1 = 13.5$ Mergs/cm³, $J_s = 9.7$ kG, and $T_c = 783$ K) [73]. We confirm the consistency between the experimental observations and the theoretical findings. Our joint efforts on $\text{Zr}_2\text{Co}_{11}$ demonstrate the efficacy of our combined approach.

C. New magnets with high magnetic anisotropy

Our combined efforts have uncovered a series of novel Fe-, Co- and Mn-rich magnetic compounds that are alloyed with magnetic or non-magnetic element X ($X = \text{N}, \text{Si}, \text{Sn}, \text{Zr}, \text{Hf}, \text{Y}, \text{C}, \text{S}, \text{Ti}, \text{or Bi}$). In these efforts, our main focus is on a non-cubic crystal structure to induce high magnetic anisotropy. Notable materials are $\text{Fe}_3\text{Co}_3\text{Ti}_2$, $\text{Fe}_3\text{Co}_3\text{Nb}_2$, $\text{Fe}_{3+x}\text{Co}_{3-x}\text{Ti}_2$ ($0 \leq x \leq 3$), Co_3N , and Co_3Si (hexagonal), Co_3N and $\text{Zr}_2\text{Co}_{11}$ (rhombohedral), $\text{Fe}_8\text{Co}_8\text{N}_2$ (tetragonal), and HfCo_7 and Fe_2CoC (orthorhombic) [7]. These compounds are free of critical rare-earth elements and expensive Pt. Most of them exhibit appreciable magnetic anisotropy ($K_1 \geq 1$ MJ/m³), large magnetization ($J_s \geq 1$ T), and high Curie temperature ($T_c \geq 300$ K).

The magnetocrystalline anisotropy, K_1 , a key intrinsic property of a magnet, plays an important role in permanent magnets and data storage. In particular, a large K_1 is desirable to develop high coercivity. The Coercivity, H_c , is ideally equivalent to the anisotropy field, H_a , and

is inversely proportional to M_s , namely,

$$H_c = H_a = 2K_1/M_s. \quad (4)$$

A permanent-magnet material should have not only a large M_s but also a sufficiently large H_a to exhibit high H_c . As mentioned in Sec. VB, magnetic materials with $\kappa \geq 1$ are promising for permanent-magnet applications. Most of the Fe-, Co-, and Mn-rich compounds found by our experimental search fall in this category, as shown in Fig. 13(a).

The energy product, $(BH)_{\max}$, a key figure of merit in permanent magnets, is defined as the maximum of the product of B and H in the second quadrant of the B - H curve, where $B = \mu_0(H + M)$ is the flux density or magnetic-field induction. The maximum theoretical energy product achievable for a magnetic material is

$$(BH)_{\max}^{\text{th}} = J_s^2/4. \quad (5)$$

Figure 13(a) shows that our new compounds have J_s of 0.75–1.25 T. These materials have the potential to exhibit room-temperature energy products of 111–318 kJ/m³ (equivalent to 14–40 MGOe), which are higher than those of the traditional rare-earth-free magnets, such as ferrites (~ 30 kJ/m³) and “alnico (~ 72 kJ/m³),” a family of alloys made of iron, aluminium, nickel and cobalt. Moreover, these values are comparable to those of rare-earth-based Sm-Co alloys (~ 239 kJ/m³). Practically, maximum room-temperature energy products of 41–162 kJ/m³ are achieved in the nanostructured films of the new rare-earth-free materials [30, 78–82], as shown in Fig. 13(b). If appropriate scale-up methods for bulk production of these new compounds are developed, these materials can be used for applications, where cost-effective magnets with the intermediate performance between alnico and rare-earth-based magnets are highly expected [71].

High uniaxial anisotropy K_u (or generally labelled as K_1) is essential to improve the thermal stability of written bits (grains) in high-density recording media [8, 9]. The potential of a magnetic material can be assessed by using the stability criterion, ξ , written as

$$\xi = K_u V / k_B T \geq 50, \quad (6)$$

where V and k_B are the volume of the grains and the Boltzmann constant, respectively. The areal density can be deduced from the thermally stable minimal grain size, D_p , of a magnetic material. In a perpendicular recording media, the grain size can be written as

$$D_p = \left[\frac{2k\xi k_B T}{H_a M_s (1 - 4\pi M_s / H_a)^2} \right]^n, \quad (7)$$

where $k = 6/\pi$ and $n = 1/3$ for spherical grains [8].

In order to explore the prospect of new magnetic compounds, we evaluate the spherical grain size, D_p , at room temperature using $\xi = 50$. Figure 14 shows a plot of the

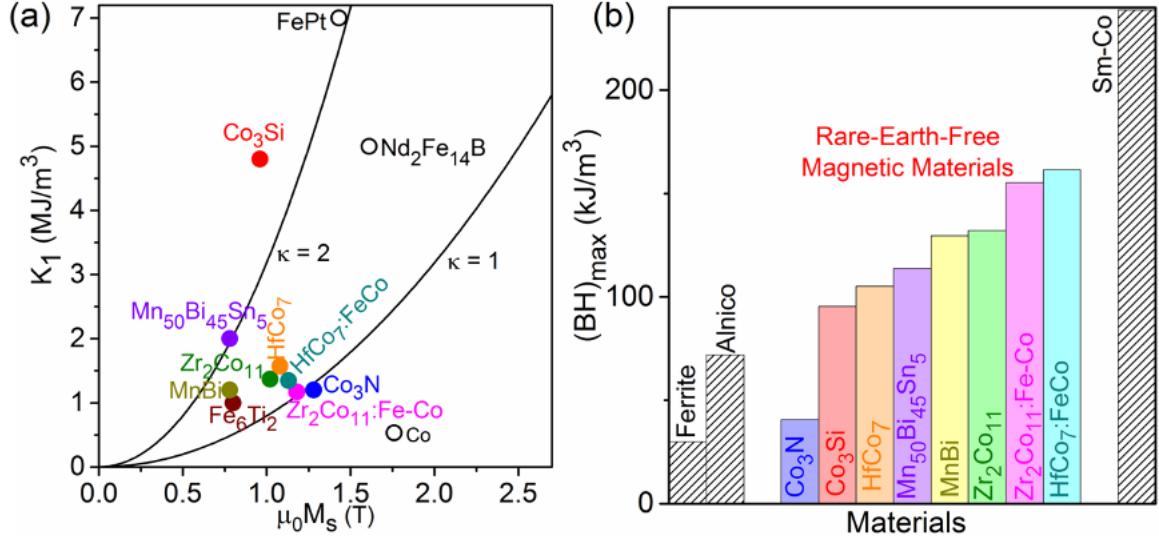


FIG. 13. Room-temperature magnetic properties of rare-earth-free magnetic materials. (a) Magnetocrystalline anisotropy constant, K_1 , versus saturation magnetic polarization $J_s = \mu_0 M_s$ (solid circles). Values of K_1 and J_s for Co, Nd₂Fe₁₄B, and L1₀-FePt are included for comparison (open circles). The parabolic curves correspond to the magnetic hardness parameters, $\kappa = 1$ and 2 are also shown. (b) Energy products of the rare-earth-free nanostructured magnetic materials are compared with those of traditional bulk magnets (gray-patterned bar graphs).

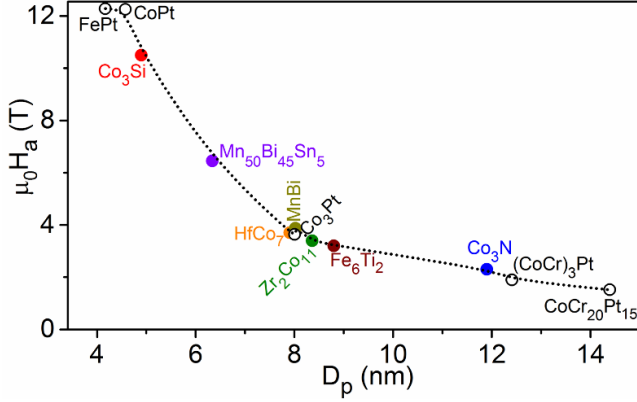


FIG. 14. Magnetic anisotropy field, $\mu_0 H_a$, versus estimated minimal stable spherical grain diameter, D_p , at room temperature for the rare-earth- and Pt-free magnetic materials (solid circles). Those values for some of the traditional Pt-based alloys are also given for comparison (open circles).

magnetic anisotropy field, $\mu_0 H_a$, as a function of the estimated D_p values. We find that the estimated D_p values of our new compounds are comparable with those of Pt-based materials. Note that the D_p values of our Pt-free compounds can be further decreased if these materials are fabricated in the form of cylindrical grains or elongated cubes. Significant research efforts have to be initiated, with help of the combined screening methods, towards the discovery of a new cost-effective materials for practical data-storage applications.

VII. PERSPECTIVES

The number of known structures of binary, ternary, and quaternary compounds available for making permanent magnets is much less than that of possible structures and compounds. There is great possibility for the discovery of new magnetic materials. Yet, it is a difficult task to predict a new structure that is viable *and* has desired magnetic properties. There will be a huge list of candidate compounds owing to a myriad of possible combinations of available elements across the periodic table. Even for a particular chemical composition (stoichiometry), there will be several polymorphs that can exist.

The use of artificial intelligence (AI) methods, such as machine-learning algorithms and neural network models, is setting the trend for the design of new advanced materials including permanent magnets [10, 11]. The basic idea behind AI-based approach is to make an instant assessment of materials properties in the hope of speeding up a whole search process. For example, researchers develop machine-learning models to find the relationship between material and its Curie temperature [83, 84]. AI-based computational screening may offer a tool to seek out promising structures from a large number of candidate structures.

In traditional computational approaches, it is essential to solve the basic equations to understand (“deduce”) material properties from first principles. In contrast, AI-assisted material discovery is a data-driven *inductive* approach. Computer needs sample data, called training data, as inputs for building a predictive AI model. Such training data can be a collection of representative data from experiments and calculations. In a machine-

learning approach, learning on database space is a very important step to help close the gap between known and predicted properties.

Basic material properties can be extracted from several open databases [12–17]. However, these databases provide little information about the magnetic properties. In particular, a serious drawback is the sparsity of the microscopic magnetic properties. Our database provides both macroscopic (“lattice-wide”) and microscopic (“site-resolved”) magnetic data suitable for AI-based design of permanent magnets. Moreover, our database contains a lot of metastable Fe-rich compounds discovered from our AGA searches. These AGA structures and their site-specific magnetic data enable us to supply plentiful data points in Fe-rich region, serving as central resources for developing machine-learning models. Such data has been scarce in other databases to date. The combination of our extensive datasets and advanced data-mining techniques makes it possible to better identify synthesizable candidate magnets that are free from critical elements.

VIII. SUMMARY

We have developed an open database specialized for magnetic materials. Our database has a number of unique features: (i) the AGA to discover new stable and metastable structures, (ii) the site-specific magnetic data from high-throughput first-principles calculations,

(iii) massive datasets for crystals and clusters, and (iv) the automated web applications in close cooperation with the online database. We have illustrated that our data-intensive methods improve efficiency of the experimental fabrication of new rare-earth- and Pt-free magnetic materials that show promising magnetic properties for permanent-magnet and data-storage applications. Our database provides a solid platform that guides the theoretical and experimental design of a new rare-earth-free magnet, especially when coupled with AI methods, such as machine learning.

ACKNOWLEDGMENTS

The authors acknowledge support from the National Science Foundation (NSF), through the Designing Materials to Revolutionize and Engineer our Future (DM-REF) program, with the award numbers of 1729202, 1729288, and 1729677. R.W. acknowledges the support from China Scholarship Council (File No. 201906340034) and the Supercomputing Center of University of Science and Technology of China. S.W. acknowledges support from the Key Projects of Basic Research of the Shanghai Municipal Science and Technology Commission (No. 18JC1411500). HPC resources were provided by the Texas Advanced Computing Center (TACC), through the Extreme Science and Engineering Discovery Environment (XSEDE) allocation.

-
- [1] J. M. D. Coey and H. Sun, Improved magnetic properties by treatment of iron-based rare earth intermetallic compounds in ammonia, *J. Magn. Magn. Mater.* **87**, L251 (1990).
 - [2] J. F. Herbst, $R_2Fe_{14}B$ materials: Intrinsic properties and technological aspects, *Rev. Mod. Phys.* **63**, 819 (1991).
 - [3] J. M. D. Coey, Permanent magnets: Plugging the gap, *Scr. Mater.* **67**, 524 (2012).
 - [4] T. Miyake, K. Terakura, Y. Harashima, H. Kino, and S. Ishibashi, First-principles study of magnetocrystalline anisotropy and magnetization in $NdFe_{12}$, $NdFe_{11}Ti$, and $NdFe_{11}TiN$, *J. Phys. Soc. Jpn.* **83**, 043702 (2014).
 - [5] T. Miyake and H. Akai, Quantum theory of rare-earth magnets, *J. Phys. Soc. Jpn.* **87**, 041009 (2018).
 - [6] J. Cui, M. Kramer, L. Zhou, F. Liu, A. Gabay, G. Hadjipanayis, B. Balasubramanian, and D. Sellmyer, Current progress and future challenges in rare-earth-free permanent magnets, *Acta Mater.* **158**, 118 (2018).
 - [7] B. Balasubramanian, M. Sakurai, C.-Z. Wang, X. Xu, K.-M. Ho, J. R. Chelikowsky, and D. J. Sellmyer, Synergistic computational and experimental discovery of novel magnetic materials, *Mol. Syst. Des. Eng.* **5**, 1098 (2020).
 - [8] C. Tannous and R. L. Comstock, Magnetic information-storage materials, in *Springer Handbook of Electronic and Photonic Materials*, edited by S. Kasap and P. Capper (Springer International Publishing, Cham, 2017) pp. 1185–1223.
 - [9] D. Weller and T. McDaniel, Media for extremely high density recording, in *Advanced Magnetic Nanostructures*, edited by D. Sellmyer and R. Skomski (Springer US, Boston, MA, 2006) pp. 295–324.
 - [10] K. T. Butler, D. W. Davies, H. Cartwright, O. Isayev, and A. Walsh, Machine learning for molecular and materials science, *Nature* **559**, 547 (2018).
 - [11] J. E. Gubernatis and T. Lookman, Machine learning in materials design and discovery: Examples from the present and suggestions for the future, *Phys. Rev. Materials* **2**, 120301 (2018).
 - [12] S. Curtarolo, W. Setyawan, G. L. Hart, M. Jahnatek, R. V. Chepulskii, R. H. Taylor, S. Wang, J. Xue, K. Yang, O. Levy, M. J. Mehl, H. T. Stokes, D. O. Demchenko, and D. Morgan, AFLOW: An automatic framework for high-throughput materials discovery, *Comput. Mater. Sci.* **58**, 218 (2012).
 - [13] <http://afloplib.org>.
 - [14] A. Jain, S. P. Ong, G. Hautier, W. Chen, W. D. Richards, S. Dacek, S. Cholia, D. Gunter, D. Skinner, G. Ceder, and K. A. Persson, Commentary: The materials project: A materials genome approach to accelerating materials innovation, *APL Materials* **1**, 011002 (2013).
 - [15] <https://materialsproject.org>.
 - [16] J. E. Saal, S. Kirklin, M. Aykol, B. Meredig, and C. Wolverton, Materials design and discovery with high-throughput density functional theory: The open quantum materials database (OQMD), *JOM* **65**, 1501 (2013).

- [17] <http://oqmd.org>.
- [18] <https://repository.nomad-coe.eu>.
- [19] <http://webbdcristal1.ehu.es/magnadata/>.
- [20] P. Nieves, S. Arapan, J. Maudes-Raedo, R. Marticorena-Sánchez, N. Del Brío, A. Kovacs, C. Echevarria-Bonet, D. Salazar, J. Weischenberg, H. Zhang, O. Vekilova, R. Serrano-López, J. Barandiaran, K. Skokov, O. Gutfleisch, O. Eriksson, H. Herper, T. Schrefl, and S. Cuesta-López, Database of novel magnetic materials for high-performance permanent magnet development, *Comput. Mater. Sci.* **168**, 188 (2019).
- [21] <http://crono.ubu.es/novamag>.
- [22] Visit <https://magmatdb.herokuapp.com/> for Magnetic Materials Database.
- [23] D. M. Deaven and K. M. Ho, Molecular geometry optimization with a genetic algorithm, *Phys. Rev. Lett.* **75**, 288 (1995).
- [24] S. Q. Wu, M. Ji, C. Z. Wang, M. C. Nguyen, X. Zhao, K. Umemoto, R. M. Wentzcovitch, and K. M. Ho, An adaptive genetic algorithm for crystal structure prediction, *J. Phys.: Condens. Matter* **26**, 035402 (2013).
- [25] P. Brommer and F. Gähler, Potfit: effective potentials from *ab initio* data, *Model. Simul. Mater. Sci. Eng.* **15**, 295 (2007).
- [26] X. Zhao, M. C. Nguyen, W. Y. Zhang, C. Z. Wang, M. J. Kramer, D. J. Sellmyer, X. Z. Li, F. Zhang, L. Q. Ke, V. P. Antropov, and K. M. Ho, Exploring the structural complexity of intermetallic compounds by an adaptive genetic algorithm, *Phys. Rev. Lett.* **112**, 045502 (2014).
- [27] X. Zhao, C.-Z. Wang, Y. Yao, and K.-M. Ho, Large magnetic anisotropy predicted for rare-earth-free $\text{Fe}_{16-x}\text{Co}_x\text{N}_2$ alloys, *Phys. Rev. B* **94**, 224424 (2016).
- [28] B. Balamurugan, B. Das, W. Y. Zhang, R. Skomski, and D. J. Sellmyer, Hf-Co and Zr-Co alloys for rare-earth-free permanent magnets, *J. Phys.: Condens. Matter* **26**, 064204 (2014).
- [29] X. Zhao, L. Ke, C.-Z. Wang, and K.-M. Ho, Metastable cobalt nitride structures with high magnetic anisotropy for rare-earth free magnets, *Phys. Chem. Chem. Phys.* **18**, 31680 (2016).
- [30] B. Balasubramanian, X. Zhao, S. R. Valloppilly, S. Benival, R. Skomski, A. Sarella, Y. Jin, X. Li, X. Xu, H. Cao, H. Wang, A. Enders, C.-Z. Wang, K.-M. Ho, and D. J. Sellmyer, Magnetism of new metastable cobalt-nitride compounds, *Nanoscale* **10**, 13011 (2018).
- [31] V. Gvozdetzkyi, G. Bhaskar, M. Batuk, X. Zhao, R. Wang, S. L. Carnahan, M. P. Hanrahan, R. A. Ribeiro, P. C. Canfield, A. J. Rossini, C.-Z. Wang, K.-M. Ho, J. Hadermann, and J. V. Zaikina, Computationally driven discovery of a family of layered LiNiB polymorphs, *Angew. Chem. Int. Ed.* **58**, 15855 (2019).
- [32] R. Wang, Y. Sun, V. Gvozdetzkyi, X. Zhao, F. Zhang, L.-H. Xu, J. V. Zaikina, Z. Lin, C.-Z. Wang, and K.-M. Ho, Theoretical search for possible Li-Ni-B crystal structures using an adaptive genetic algorithm, *J. Appl. Phys.* **127**, 094902 (2020).
- [33] P. Hohenberg and W. Kohn, Inhomogeneous electron gas, *Phys. Rev.* **136**, B864 (1964).
- [34] W. Kohn and L. J. Sham, Self-consistent equations including exchange and correlation effects, *Phys. Rev.* **140**, A1133 (1965).
- [35] P. E. Blöchl, Projector augmented-wave method, *Phys. Rev. B* **50**, 17953 (1994).
- [36] J. P. Perdew, K. Burke, and M. Ernzerhof, Generalized gradient approximation made simple, *Phys. Rev. Lett.* **77**, 3865 (1996).
- [37] H. J. Monkhorst and J. D. Pack, Special points for brillouin-zone integrations, *Phys. Rev. B* **13**, 5188 (1976).
- [38] G. Kresse and J. Furthmüller, Efficiency of *ab-initio* total energy calculations for metals and semiconductors using a plane-wave basis set, *Comput. Mater. Sci.* **6**, 15 (1996).
- [39] G. Kresse and J. Furthmüller, Efficient iterative schemes for *ab initio* total-energy calculations using a plane-wave basis set, *Phys. Rev. B* **54**, 11169 (1996).
- [40] P. Giannozzi, S. Baroni, N. Bonini, M. Calandra, R. Car, C. Cavazzoni, D. Ceresoli, G. L. Chiarotti, M. Cococcioni, I. Dabo, A. D. Corso, S. de Gironcoli, S. Fabris, G. Fratesi, R. Gebauer, U. Gerstmann, C. Gougoussis, A. Kokalj, M. Lazzeri, L. Martin-Samos, N. Marzari, F. Mauri, R. Mazzarello, S. Paolini, A. Pasquarello, L. Paulatto, C. Sbraccia, S. Scandolo, G. Sclauzero, A. P. Seitsonen, A. Smogunov, P. Umari, and R. M. Wentzcovitch, QUANTUM ESPRESSO: a modular and open-source software project for quantum simulations of materials, *J. Phys.: Condens. Matter* **21**, 395502 (2009).
- [41] A. Liechtenstein, M. Katsnelson, V. Antropov, and V. Gubanov, Local spin density functional approach to the theory of exchange interactions in ferromagnetic metals and alloys, *J. Magn. Magn. Mater.* **67**, 65 (1987).
- [42] O. K. Andersen, Linear methods in band theory, *Phys. Rev. B* **12**, 3060 (1975).
- [43] M. van Schilfgaarde and V. P. Antropov, First-principles exchange interactions in Fe, Ni, and Co, *J. Appl. Phys.* **85**, 4827 (1999).
- [44] D. Pashov, S. Acharya, W. R. Lambrecht, J. Jackson, K. D. Belashchenko, A. Chantis, F. Jamet, and M. van Schilfgaarde, Questaal: A package of electronic structure methods based on the linear muffin-tin orbital technique, *Comput. Phys. Commun.* **249**, 107065 (2020).
- [45] M. Sakurai, X. Zhao, C.-Z. Wang, K.-M. Ho, and J. R. Chelikowsky, Influence of nitrogen dopants on the magnetization of Co_3N clusters, *Phys. Rev. Materials* **2**, 024401 (2018).
- [46] M. L. Tiago, Y. Zhou, M. M. G. Alemany, Y. Saad, and J. R. Chelikowsky, Evolution of magnetism in iron from the atom to the bulk, *Phys. Rev. Lett.* **97**, 147201 (2006).
- [47] J. Souto-Casares, M. Sakurai, and J. R. Chelikowsky, Structural and magnetic properties of large cobalt clusters, *Phys. Rev. B* **93**, 174418 (2016).
- [48] M. Sakurai, J. Souto-Casares, and J. R. Chelikowsky, Size dependence of structural stability and magnetization of nickel clusters from real-space pseudopotentials, *Phys. Rev. B* **94**, 024437 (2016).
- [49] R. H. Byrd, P. Lu, J. Nocedal, and C. Zhu, A limited memory algorithm for bound constrained optimization, *SIAM J. Sci. Comput.* **16**, 1190 (1995).
- [50] C. Zhu, R. H. Byrd, P. Lu, and J. Nocedal, Algorithm 778: L-BFGS-B: Fortran subroutines for large-scale bound-constrained optimization, *ACM Trans. Math. Software* **23**, 550 (1997).
- [51] J. L. Morales and J. Nocedal, Remark on “algorithm 778: L-BFGS-B: Fortran subroutines for large-scale bound constrained optimization”, *ACM Trans. Math. Software* **38**, 1 (2011).
- [52] J. R. Chelikowsky, N. Troullier, and Y. Saad, Finite-difference-pseudopotential method: Electronic structure calculations without a basis, *Phys. Rev. Lett.* **72**, 1240

- (1994).
- [53] J. R. Chelikowsky, N. Troullier, K. Wu, and Y. Saad, Higher-order finite-difference pseudopotential method: An application to diatomic molecules, *Phys. Rev. B* **50**, 11355 (1994).
 - [54] L. Kronik, A. Makmal, M. L. Tiago, M. M. G. Alemany, M. Jain, X. Huang, Y. Saad, and J. R. Chelikowsky, PARSEC – the pseudopotential algorithm for real-space electronic structure calculations: recent advances and novel applications to nano-structures, *Phys. Status Solidi B* **243**, 1063 (2006).
 - [55] M. Sakurai and J. R. Chelikowsky, Enhanced magnetic moments in Mn-doped FeCo clusters owing to ferromagnetic surface Mn atoms, *Phys. Rev. Materials* **3**, 044402 (2019).
 - [56] Y. Zhou, Y. Saad, M. L. Tiago, and J. R. Chelikowsky, Parallel self-consistent-field calculations via Chebyshev-filtered subspace acceleration, *Phys. Rev. E* **74**, 066704 (2006).
 - [57] Y. Zhou, Y. Saad, M. L. Tiago, and J. R. Chelikowsky, Self-consistent-field calculations using Chebyshev-filtered subspace iteration, *J. Comput. Phys.* **219**, 172 (2006).
 - [58] Y. Zhou, J. R. Chelikowsky, and Y. Saad, Chebyshev-filtered subspace iteration method free of sparse diagonalization for solving the Kohn–Sham equation, *J. Comput. Phys.* **274**, 770 (2014).
 - [59] <https://www.iucr.org/resources/cif>.
 - [60] <https://yaml.org>.
 - [61] <https://www.python.org>.
 - [62] <https://pymatgen.org>.
 - [63] <https://www.mongodb.com>.
 - [64] <https://palletsprojects.com/p/flask>.
 - [65] <https://palletsprojects.com/p/jinja>.
 - [66] <https://www.heroku.com>.
 - [67] <https://matplotlib.org>.
 - [68] <https://www.iucr.org>.
 - [69] <https://lammmps.sandia.gov>.
 - [70] <https://www.json.org>.
 - [71] R. Skomski and J. M. D. Coey, Magnetic anisotropy — how much is enough for a permanent magnet?, *Scripta Mater.* **112**, 3 (2016).
 - [72] G. H. O. Daalderop, P. J. Kelly, and M. F. H. Schuurmans, Magnetocrystalline anisotropy of YCo_5 and related RECo_5 compounds, *Phys. Rev. B* **53**, 14415 (1996).
 - [73] B. Balamurugan, B. Das, W. Y. Zhang, R. Skomski, and D. J. Sellmyer, Hf–Co and Zr–Co alloys for rare-earth-free permanent magnets, *J. Phys.: Condens. Matter* **26**, 064204 (2014).
 - [74] B. G. Demczyk and S. F. Cheng, Structures of $\text{Zr}_2\text{Co}_{11}$ and HfCo_7 intermetallic compounds, *J. Appl. Cryst.* **24**, 1023 (1991).
 - [75] A. Gabay, Y. Zhang, and G. Hadjipanayis, Cobalt-rich magnetic phases in Zr–Co alloys, *J. Magn. Magn. Mater.* **236**, 37 (2001).
 - [76] G. Ivanova, N. Shchegoleva, and A. Gabay, Crystal structure of $\text{Zr}_2\text{Co}_{11}$ hard magnetic compound, *J. Alloys Compd.* **432**, 135 (2007).
 - [77] G. Ivanova and N. Shchegoleva, The microstructure of a magnetically hard $\text{Zr}_2\text{Co}_{11}$ alloy, *Phys. Metals Metallogr.* **107**, 270 (2009).
 - [78] B. Balasubramanian, P. Manchanda, R. Skomski, P. Mukherjee, S. R. Valloppilly, B. Das, G. C. Hadjipanayis, and D. J. Sellmyer, High-coercivity magnetism in nanostructures with strong easy-plane anisotropy, *Appl. Phys. Lett.* **108**, 152406 (2016).
 - [79] W. Zhang, B. Balasubramanian, P. Kharel, R. Pahari, S. R. Valloppilly, X. Li, L. Yue, R. Skomski, and D. J. Sellmyer, High energy product of MnBi by field annealing and Sn alloying, *APL Materials* **7**, 121111 (2019).
 - [80] B. Balasubramanian, B. Das, R. Skomski, W. Y. Zhang, and D. J. Sellmyer, Magnetic materials: Novel nanostructured rare-earth-free magnetic materials with high energy products (adv. mater. 42/2013), *Adv. Mater.* **25**, 6089 (2013).
 - [81] B. Balasubramanian, P. Mukherjee, R. Skomski, P. Manchanda, B. Das, and D. J. Sellmyer, Magnetic nanostructuring and overcoming brown’s paradox to realize extraordinary high-temperature energy products, *Sci. Rep.* **4**, 6265 (2014).
 - [82] W. Zhang, P. Kharel, S. Valloppilly, L. Yue, and D. J. Sellmyer, High-energy-product MnBi films with controllable anisotropy, *Phys. Status Solidi B* **252**, 1934 (2015).
 - [83] H. C. Dam, V. C. Nguyen, T. L. Pham, A. T. Nguyen, K. Terakura, T. Miyake, and H. Kino, Important descriptors and descriptor groups of curie temperatures of rare-earth transition-metal binary alloys, *J. Phys. Soc. Jpn.* **87**, 113801 (2018).
 - [84] J. Nelson and S. Sanvito, Predicting the curie temperature of ferromagnets using machine learning, *Phys. Rev. Materials* **3**, 104405 (2019).